THE ROLE OF THE NATURE OF PILLARS IN THE STRUCTURAL AND MAGNETIC PROPERTIES OF MAGNETIC PILLARED CLAYS

Cherifa Bachir[1,2,*], Yanhua Lan[3], Valeriu Mereacre[3], Annie K. Powell[3], Christian Bender Koch[4], and Peter G. Weidler[5]

[1] Department of Industrial Chemistry, Faculty of Sciences, B.P. 1505 EL-Mnaouer, University of Sciences and Technologies USTO "Mohamed Boudiaf," Oran, Algeria
[2] Chemistry Materials Laboratory, Department of Chemistry, Faculty of Science, University of Oran Es-Senia, B.P 1524 El-M'Naouer, Oran, Algeria
[3] Institute for Inorganic Chemistry, Karlsruher Institut für Technologie KIT, Engesserstr. 15 Geb. 30.45, D-76131 Karlsruhe, Germany
[4] Department of Basic Sciences and Environment, Faculty of Life Sciences, University of Copenhagen, Thorvaldsensvej 40, DK-1871 Frederiksberg, Denmark
[5] Institute of Functional Interfaces, Karlsruher Institut für Technologie KIT, Hermann-von-Helmholtz-Platz 1, D-76344 Eggenstein-Leopoldshafen, Germany

Abstract—Pillared clays (PILCs) with magnetic properties have significant potential for application in industry and the environment, but relatively few studies of these types of materials have been carried out. The aim of the present work was to gain insight into the magnetic and structural properties of pillared clays by examining in detail the influence of the calcination temperature and the nature of different pillared clays on these properties.

Magnetic layered systems from different pillared clays were prepared and characterized. Firstly, Ti-, Al-, and Zr-pillared clays (Ti-PILCs, Al-PILCs, and Zr-PILCs, respectively) were produced at different calcination temperatures and then magnetic pillared clays (Ti-M-PILCs, Al-M-PILCs, and Zr-M-PILCs) were prepared at ambient temperature. The synthesis involves a reduction in aqueous solution of the original Fe-exchanged pillared clay using $NaBH_4$. The structural properties of pillared clays and their magnetic forms were investigated using X-ray diffraction, N_2 adsorption, cation exchange capacity determination, and X-ray fluorescence (XRF) measurements. The properties of the magnetic pillared clays were investigated by superconducting quantum interference devices and Mössbauer spectroscopy. An evaluation of the data obtained allowed an estimation of the pillared structure in one PILC-model before and after magnetization. The model was determined on the basis of a simple geometric model and experimental data leading to the calculation of a filling factor (FF) which contained information about the number of intercalated pillared layers and the unaffected layers. In the case of Ti precursors, the best calcination temperature was 400ºC, which maintained the highest specific surface area and pore volume with magnetic parameters suitable for magnetic application. Similar experiments with Al- and Zr-pillars have been discussed. A correlation between the XRF data, porosity, FF calculation, and magnetic properties led to the conclusion that the sample Al-M-PILC previously calcined at 500ºC was the most stable material after the magnetization process. The same examination in the case of Zr materials suggested that the most stable sample had been calcined at 300ºC (sample Zr-M-PILC-300).

Key Words—Filling Factor, Magnetic Pillared Clays, Mössbauer Spectroscopy, Pillared Clays, SQUID.

INTRODUCTION

Combination of interesting adsorption properties of materials, especially clays, with magnetic properties to produce novel adsorbents is very attractive. These materials are promising new magnetic carriers suitable for a range of applications such as magnetic separation. Magnetic particles can be used to adsorb contaminants from aqueous effluents and after the adsorption is carried out, the adsorbent can be separated from the medium by a simple magnetic process. Preliminary studies have been carried out by Oliveira *et al.* (2002, 2003), Mak and Chen (2004), and Belessi *et al.* (2009).

Relatively few studies of magnetic pillared clays have been carried out to date (Skoutelas *et al.*, 1999; Bachir *et al*, 2009; Yu and Yang, 2010). The performance of the magnetically modified Fe-pillared clay mineral was evaluated by adsorption of methyl orange and, intensified separation by means of an external magnetic field. Excellent performance in terms of adsorption and magnetic separation suggests that this material has real potential for chemical engineering and environmental-pollution control purposes (Yu and Yang, 2010).

In another application, Mojović *et al.* (2010) used the pillaring method for paramagnetic metal encapsulation

in bentonites as a new contrast agent for digestive tract magnetic resonance imaging.

In order to maintain the porous structure of pillared clays and to avoid the predominance of non-magnetic Fe phases, only solutions with low Fe concentrations have been investigated. In previous work on magnetic properties of Ti-pillared clay, the relations between porosity, cation exchange capacity (CEC), and the magnetic properties upon Fe-intercalation, and subsequent reduction by $NaBH_4$, were investigated (Bachir *et al.*, 2009). Large CEC values combined with large porosity and specific surface area led to an even distribution of Fe in the interlayer, causing dilution of the magnetic moments and preventing long-range magnetic ordering. Samples with smaller CEC and porosity values led to clustering and the formation of magnetic units. In addition, the data strongly suggest the presence of a poorly ordered FeB alloy.

In the present study, further investigations of Ti-M-PILCs were conducted and compared with Al- and Zr-M-PILCs produced by the same experiment. The influence of the calcination temperature and the pillar nature for each set of experiments was examined. The importance of non-intercalated layers and the distribution of the PILC-layers on magnetic properties were also determined. Using structural data from X-ray diffraction (XRD), XRF, and porosity, a single PILC model, based on a simple geometric model, was proposed and used to calculate the number of intercalated *vs.* unaffected clay interlayers (the filling factor).

MATERIALS AND METHODS

Materials

The starting material was Na-SWy-2 (from the Source Clays Repository of The Clay Minerals Society), obtained by the treatment reported by Bachir *et al.* (2009). The Al pillaring solution was prepared by a 0.225 M NaOH solution added dropwise with vigorous stirring to a 0.5 M $AlCl_3.6H_2O$ solution. The amount of NaOH added was calculated in order to obtain an OH/Al molar ratio of 2. This solution was aged for 24 h. The montmorillonites were intercalated by slow addition of corresponding amounts of pillaring solution to the suspension of Na-SWy-2 montmorillonite under stirring in order to obtain 10 mmol of Al/g clay. The Zr-pillared clays, Zr-PILCs, were prepared using a freshly prepared 0.1 M $ZrOCl_2.8H_2O$ as the pillaring solution (Yamanaka and Brindley, 1979; Bartley and Burch, 1985; Chaabene *et al.*, 2004). The intercalated Zr-montmorillonite was prepared by slow addition of corresponding amounts of prepared pillaring solution to the Na-SWy-2 suspension, with stirring, in order to obtain 10 mmol of Zr/g of clay. Titanium-pillared clays (Ti-PILCs) were prepared according to the method of Sterte (1986). The mixtures obtained were separated by centrifugation, washed with distilled water, and dried at 60ºC. The intercalated solids obtained

were calcined at different temperatures (200−500ºC) in air at a heating rate of 1ºC/min from room temperature up to the calcination temperature for 4 h (Al-PILCs, Elmchaouri and Mahboub, 2005), 2 h (Zr-PILCs, Mishra and Rao, 2005), and 3 h (Ti-PILCs, Sterte, 1986).

Magnetic properties were imparted to the pillared clays (Zhang and Manthiram, 1996) by ion exchange of the present interlayer ions with an excess of ferrous Fe (0.2 M $FeCl_2.4H_2O$) solution and stirring on a magnetic stirrer for 24 h. The products were centrifuged and washed with distilled water several times until chloride-free and dried at 60ºC. Iron-exchanged PILCs (1 g) was then suspended in 50 mL of deionized water and stirred. A freshly prepared solution of 0.5 M $NaBH_4$ (25 mL) was added slowly to the suspension at room temperature. This product was stirred for 1 h, separated, freeze-dried, and stored in a desiccator.

Room-temperature magnetic samples were prepared in the present study for use in adsorption experiments; the efficiency of the magnetic materials has already been tested in this application and the results were successful (in prep.).

The original pillared samples were designated as Cation-PILC, followed by the corresponding calcination temperature (Cation-PILC-temperature [ºC]). For the magnetic pillared samples the notation Cation-M-PILC-temperature was used (M for magnetic).

Methods

X-ray diffraction was carried out on a Bruker D5000 diffractometer equipped with a graphite diffracted-beam monochromator and CuKα radiation (λ = 1.5418 Å) at 40 kV and 40 mA. Oriented clay-aggregate specimens were prepared by drying clay suspensions on glass slides. X-ray diffraction patterns were recorded over the range 2−12º2θ (step size, 0.02º2θ; step time, 4 s) for glass slide samples. Qualitative phase analysis was carried out for the powder samples (2−72º2θ; step size, 0.025º2θ; step time, 10 s) using Brindley and Brown (1980) and *Diffrac Plus evaluation* 10.0 software provided by Bruker AXS.

Nitrogen-adsorption measurements were performed using a Quantachrome Autosorb-1MP instrument in the relative pressure range P/P_0 from 10^{-5} to 1. The samples were outgassed overnight at 110ºC prior to the adsorption analysis. Specific surface areas were calculated according to the BET equation (Brunauer *et al.*, 1938). The non-local density functional theory (NLDFT) was used to calculate total pore volume (V_p at $P/P_0 = 0.7$, pore-width filled ~7 nm; based on the specific surface area and the deduced particle size, larger pore widths were attributed to interparticle pores and, hence, were assumed to make no contribution to the particle pore volume); micropore volume (V_{mp}, width <2 nm); and mesopore volume ($V_{mes} = V_p - V_{mp}$, pore width = 2−7 nm) from the adsorption branch assuming cylindrical pore geometry.

X-ray fluorescence measurements were performed using a MagiXPRO spectrometer from Philips, equipped with a Rh X-ray tube, on air-dry powdered samples fused with lithium tetraborate. The chemical composition reported as wt.% oxides of pillared clays was important in determining the additional amount of intercalated element and the amount of additional Fe of the magnetic pillared clays. The loss on ignition (LOI) was determined separately by heating a sample in an oven at 1000ºC for 2 h.

The structural formula of the parent clay was calculated from the chemical composition according to Köster (1977) after measuring the layer charge, which was determined by the alkylammonium method (Lagaly, 1994). Textured samples were obtained by dispersion in ethanol together with a small amount of talc used as an XRD line standard. After drying, the samples were stored in a desiccator over P_2O_5 until their basal spacings were recorded by XRD (Rühlicke and Kohler, 1981). The layer charge (ξ) was calculated as recommended by Olis $et\ al.$ (1990) using the basal spacing of the dodecylammonium derivative ($n_c = 12$):

$$\xi = (d_{001} - 5.52)/32.98 \tag{1}$$

The CEC was measured by Cu-triethylenetetramine exchange according to Meier and Kahr (1999). The concentration of Cu-triethylenetetramine complex, $[Cu(trien)]^{2+}$, was determined by photometry (λ = 580 nm) in the clear supernatant using a Genesys 10 UV-Vis Spectrophotometer.

The magnetic measurements were carried out using a Quantum Design SQUID (superconducting quantum interference device) magnetometer MPMS-XL, which was operated between 1.8 and 400 K with dc-applied magnetic fields ranging from −7 to 7 T. Measurements were performed on a polycrystalline sample placed in a plastic container.

The mass of the samples used for measurements was between 10 and 13 mg. A detailed description of the hysteresis curves, their parameters, and the ZFC/FC measurements was given by Bachir $et\ al.$ (2009).

Mössbauer spectra were acquired using a conventional spectrometer in constant acceleration mode equipped with a ^{57}Co source (3.7 GBq) in a Rh matrix. Isomer shifts were given relative to the centroid of the spectrum of α-Fe at room temperature. The sample was inserted inside an Oxford Instruments Mössbauer-Spectromag 4000 Cryostat which established the sample temperature at 3 or 300 K.

Calculation of the filling factor

A filling factor (FF) was calculated in order to estimate whether all the interlayer space was pillared. The calculation was carried out for Ti-PILCs, Al-PILCs, Zr-PILCs, and their magnetic forms.

Two approaches were used to determine the FF. For the first, where T = unpillared package, P = PILC package, (where package is the arrangement of two layers of montmorillonite) the focus was placed on the computation of the theoretical interlayer volume, V_{ILtheo}, taking into account the unit-cell parameters of Na-SWy-2 and the interlayer spacing, d_{IL}, deduced from the d_{001} basal spacing of the corresponding pillared clays. The second approach was based on the calculation of the pillar volume, V_{PL}, using the density of the pillar material (calculated below in the XRD investigation, Figure 1) and the additional pillar content normalized to the Na-SWy-2 content.

The value for V_{PL} obtained was added to the pore volume, V_p, at $P/P_0 = 0.7$ (pore width $\leqslant$ 7 nm) to obtain the required experimental interlayer volume, V_{ILexp}.

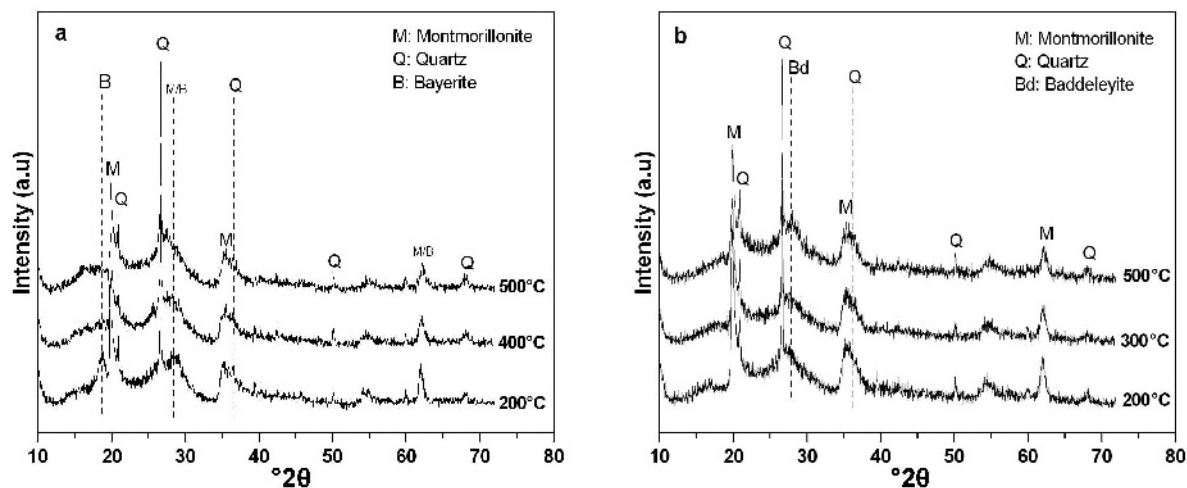The FF is given by:

$$FF = V_{ILexp}/V_{ILtheo} \tag{2}$$

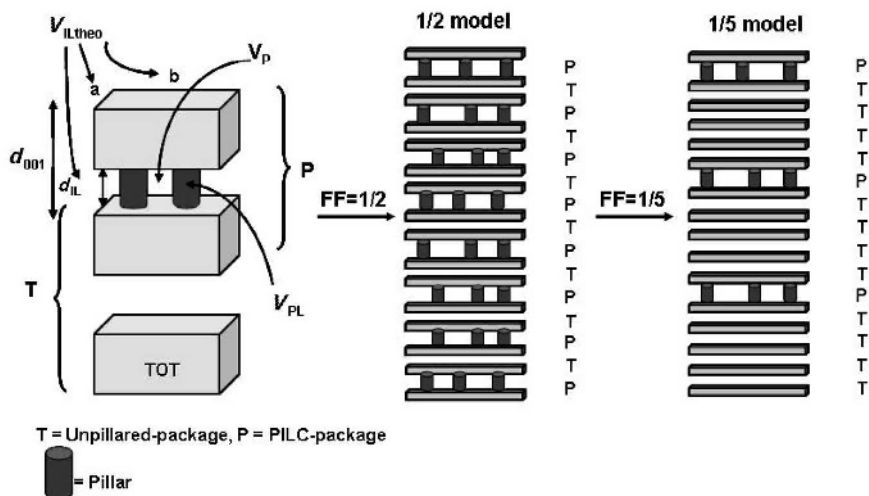Figure 1. Powder XRD patterns of (a) Al-PILCs and (b) Zr-PILCs.

Figure 2. Calculation of the filling factor.

with V_{ILtheo}, based on the unit-cell formula of Na-SWy-2, defined as:

$$V_{ILtheo} = (d_{IL}*a*b)*N_A/M \qquad (3)$$

and V_{ILexp} defined as:

$$V_{ILexp} = V_{PL} + V_p \qquad (4)$$

where d_{IL}: is the interlayer space ($d_{IL} = d_{001} - t$, where t is the TOT layer thickness); a, b are the unit-cell dimensions of 5.15 Å and 8.98 Å, respectively; N_A is Avogadro's number (6.023×10^{23}); M is the molecular weight of Na-SWy-2; V_{PL} is the pillar volume; and V_p is the pore volume at $P/P_0 = 0.7$ (pore width $\leqslant 7$ nm).

The corresponding intercalation factor (IF) can be deduced from the FF factor as follows:

$$IF = 1/FF \qquad (5)$$

Two examples of pillared structure, with FF = 1/2 and FF = 1/5 were presented (Figure 2). In the first example, 1/2 means that, in two packages T, one package P is filled with pillars. For the other model with a smaller filling factor (1/5 model), in five packages T, only one package P is filled with pillars.

RESULTS AND DISCUSSION

The chemical composition (Table 1) was combined with the measured layer charge to calculate the structural formula of the starting clay Na-SWy-2:

$$Na^+_{0.27}Ca^{2+}_{0.02}K^+_{0.01}(Si_{3.91}Al^{3+}_{0.09})(Al^{3+}_{1.55}Fe^{3+}_{0.21}Mg^{2+}_{0.25})[O_{10}(OH)_2]$$

This formula was used in the computation of the molecular weight of Na-SWy-2.

XRD investigation

The parent clay Na-SWy-2 has a Bragg peak at ~7°2θ with basal spacing of 1.24 nm. This diffraction peak was

shifted to lower 2θ values for all samples, indicating an expansion in the layer structure as a result of pillaring (Figure 3a, Table 2). The XRD patterns of the Ti materials were reported by Bachir *et al.* (2009). After Fe exchange and $NaBH_4$ reduction, a collapse of the basal spacing was observed (Figure 3b, Table 3). The decrease in basal spacing after magnetization can be explained by the reduction in the octahedral Fe(III) of the original clay. Rozenson and Heller-Kallai (1976) reported the reduction of Fe(III) in octahedral positions of smectites upon treatment with hydrazine and dithionite.

The qualitative phase analysis revealed the presence of different pillar oxides. For Ti-PILCs the powder XRD pattern revealed peaks attributable to anatase as well as quartz and montmorillonite (Bachir *et al.*, 2009). For Al-PILCs, the powder XRD patterns revealed the presence

Table 1. Chemical composition and selected properties of Na-SWy-2.

Chemical composition (oxide wt.%)		— Properties —	
SiO_2	60.42	d_{001} (nm)	1.24
Al_2O_3	19.79	SSA (m²/g)	50
Fe_2O_3	3.99	ξ (eq/mol)	0.3
MnO	0.01	CEC (meq/100 g)	85
MgO	2.34	M (g/mol)	746.83
CaO	0.13		
Na_2O	2.21		
K_2O	0.11		
TiO_2	0.11		
LOI	10.85		

d_{001}: basal spacing, SSA: specific surface area, ξ: layer charge, CEC: cation exchange capacity, M: molecular weight, LOI: loss on ignition

of a peak attributable to the bayerite (Al(OH)$_3$) 001 peak (Figure 1a). The intensity of this peak decreased with increasing calcination temperature, until its disappearance at 400ºC. As reported in the literature (Levin and Brandon, 1998), when heated in air, the bayerite transformed to boehmite (γ-AlOOH) which transformed to α-Al$_2$O$_3$. At all calcination temperatures, the powder XRD of Zr-PILCs contained a peak at ~28º2θ, which can be attributed to the diffraction peak ($\bar{1}$11) of baddeleyite (ZrO$_2$) (Figure 1b). Densities of 3.9 g cm^{-3} for anatase (TiO$_2$), 2.53 g cm^{-3} for bayerite (Al(OH)$_3$), 3.99 g cm^{-3} for alpha alumina (α-Al$_2$O$_3$), and 5.75 g cm^{-3} for baddeleyite (ZrO$_2$) for Ti-PILCs, Al-PILCs, and Zr-PILCs, respectively, and their magnetic forms, were used in the FF calculations.

SSA, porosity, and CEC determination

The specific surface area (SSA), pore volume (V_p), and meso- and micropore volumes of the original pillared materials (Table 2) revealed that all samples showed greater surface areas and porosity than the starting material, Na-SWy-2, which has a SSA of 50 m^2/g. The SSA decreased with increasing temperature. In the case of Al-PILCs, the formation of new pores, mostly micropores after pillaring, was responsible for the increase in the surface areas. The mesoporosity also contributed to the total pore volume, especially at higher temperature. Heating at 500ºC decreased the SSA to 105 m^2/g for Zr-PILCs; this behavior was accompanied by a decrease in pore volume, mostly in micropore volume, indicating a low thermal stability of the Zr-PILCs clay at this temperature. For Ti-PILCs which has the largest SSA and V_p, heating up to 600ºC transformed the polycations into oxide pillars and had no significant impact on the SSA, indicating good thermal stability of the Ti-PILC clays. In addition, an increase in the adsorbed volume, which was more pronounced in the mesopore range, was also noted (Table 2).
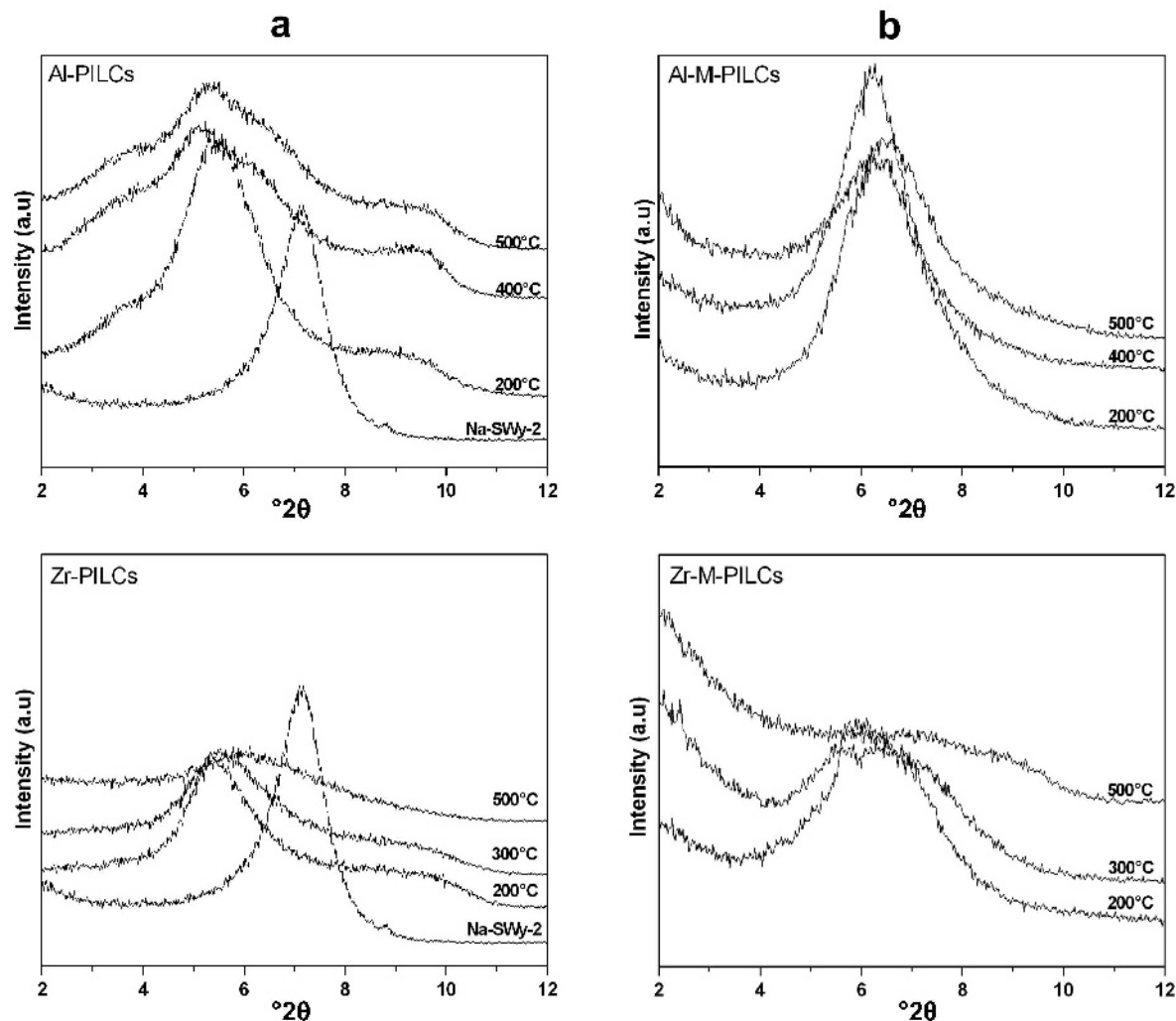

Figure 3. XRD patterns of oriented (a) Al- and Zr-pillared clay and (b) the corresponding magnetic pillared clays.

Table 2. Basal spacing (d_{001}), specific surface area (SSA), pore volume (V_p), and cation exchange capacity (CEC) of pillared clays.

Samples	d_{001} (nm)	SSA (m²/g)	V_{mp} (cm³/g)	V_{mes} (cm³/g)	V_p (cm³/g)	CEC (meq/100 g)
Al-PILC-200	1.62	220	0.074	0.032	0.106	42
Al-PILC-400	1.73	183	0.048	0.055	0.103	24
Al-PILC-500	1.66	180	0.043	0.060	0.103	18
Zr-PILC-200	1.63	175	0.051	0.042	0.093	51
Zr-PILC-300	1.61	166	0.046	0.045	0.091	48
Zr-PILC-500	1.50	105	0.022	0.041	0.063	25
Ti-PILC-200	2.80	280	0.017	0.154	0.171	25
Ti-PILC-400	2.65	262	0.010	0.151	0.161	15
Ti-PILC-500	2.50	231	0.005	0.154	0.159	13

V_{mp}: micropore volume, V_{mes}: mesopore volume.

After the magnetization process, the values of SSA and pore volume (Table 3) decreased, especially in the microporous range. This decrease was more accentuated in the case of Al-M-PILC-200, Zr-M-PILC-200, and Ti-M-PILC-200. The reduction in SSA and porosity was different for each element and each calcination temperature. The samples with the smallest reductions in SSA and porosity in each series were Al-M-PILC-500, Zr-M-PILC-300, and Ti-M-PILC-400.

In general terms, the CEC of the pillared materials decreased after pillaring with increasing calcination temperature (Table 2).

X-ray fluorescence

The magnetization process, Fe intercalation, and subsequent reduction by $NaBH_4$ increased the Fe content (Table 3). Note that the additional Fe content of Al-M-PILCs samples was different for each sample. The samples Al-M-PILC-200 and Al-M-PILC-400 had greater additional Fe content than sample Al-M-PILC-500. The additional Fe content of Zr-M-PILCs, which was responsible for the magnetic properties, was ~2% for Zr-M-PILC-200 and Zr-M-PILC-300, and ≤1% for

Zr-M-PILC-500. The additional Fe content of Ti-M-PILCs was fairly constant for all samples and did not exceed 2%. The additional pillar oxide content based on the composition of Na-SWy-2 was deduced for all the original pillared clays and their magnetic forms (Table 4) and was used in the calculation of the FF (see below).

Magnetic properties

Hysteresis curves (2, 5, 10, 50, 100, and 300 K). Only the hysteresis curves of Al-M-PILC-200 (same shape as Al-M-PILC-400), Al-M-PILC-500, Zr-M-PILC-300 (same shape as Zr-M-PILC-200), Zr-M-PILC-500, Ti-M-PILC-200, and Ti-M-PILC-400 (same shape as Ti-M-PILC-500) revealed that the Al-M-PILC samples exhibited hysteresis at all temperatures, whereas the hysteresis area was smallest for sample Al-M-PILC-500. Samples Zr-M-PILC-300 and Ti-M-PILC-400 showed hysteresis at all measurement temperatures and was more pronounced in the former. For Zr-M-PILC-500 and Ti-M-PILC-200, little hysteresis was observed at all measured temperatures. Thus, in all the samples except Ti-M-

Table 3. Basal spacing (d_{001}), specific surface area (SSA), pore volume (V_p), and amount of additional Fe of M-PILCs.

Samples	d_{001} (nm)	SSA (m²/g)	SSA reduction* (%)	V_{mp} (cm³/g)	V_{mes} (cm³/g)	V_p (cm³/g)	V_p reduction* (%)	$Fe_2O_3^\#$ (wt.%)
Al-M-PILC-200	1.40	16	93	0.000	0.014	0.014	87	3.85
Al-M-PILC-400	1.42	37	80	0.003	0.027	0.030	71	3.58
Al-M-PILC-500	1.36	77	57	0.014	0.034	0.048	53	2.35
Zr-M-PILC-200	1.42	10	94	0.000	0.008	0.008	91	2.15
Zr-M-PILC-300	1.45	123	26	0.029	0.041	0.070	23	2.09
Zr-M-PILC-500	1.20	43	59	0.003	0.030	0.033	48	0.56
Ti-M-PILC-200	1.70	137	51	0.006	0.092	0.098	42	1.85
Ti-M-PILC-400	1.57	211	20	0.007	0.129	0.136	15	1.62
Ti-M-PILC-500	1.37	175	28	0.004	0.110	0.114	28	1.86

V_{mp}: micropore volume, V_{mes}: mesopore volume, * reduction in SSA and V_p related to PILCs, # additional Fe_2O_3 content after magnetization based on the composition of M-PILCs.

Table 4. Al_2O_3 contents of Al-M-PILCs and Al-PILCs, ZrO_2 content of Zr-M-PILCs and Zr-PILCs, and TiO_2 contents of Ti-M-PILCs and Ti-PILCs.

Al samples	Al_2O_3* (wt.%)	Zr-samples	$ZrO_2^{\#}$ (wt.%)	Ti samples	TiO_2^{+} (wt.%)
Al-PILC-200	8.72	Zr-PILC-200	13.74	Ti-PILC-200	49.44
Al-PILC-400	8.67	Zr-PILC-300	13.80	Ti-PILC-400	49.43
Al-PILC-500	8.67	Zr-PILC-500	14.03	Ti-PILC-500	49.42
Al-M-PILC-200	6.07	Zr-M-PILC-200	12.95	Ti-M-PILC-200	49.01
Al-M-PILC-400	6.48	Zr-M-PILC-300	13.58	Ti-M-PILC-400	49.93
Al-M-PILC-500	7.47	Zr-M-PILC-500	13.89	Ti-M-PILC-500	50.95

* additional content based on the composition of Na-SWy-2 given as g of Al_2O_3 per 100 g of Na-SWy-2
# content based on the composition of Na-SWy-2 given as g of ZrO_2 per 100 g of Na-SWy-2
+ additional content based on the composition of Na-SWy-2 given as g of TiO_2 per 100 g of Na-SWy-2

PILC-200 and Zr-M-PILC-500 a ferro- or ferrimagnetic behavior was suggested. The saturation magnetization, M_s, increased further with decreasing temperature for all samples.

Saturation magnetization, M_s, at room temperature. Values for M_s at room temperature were deduced from the hysteresis curves for the various samples and normalized to the additional Fe content after magnetization (Table 5).

The value of M_s for each M-PILC sample, was compared with values reported for magnetite, maghemite, Fe, and Fe_xB reported by Moskowitz (1991) and Zhang *et al.* (2001). The comparison revealed the presence of Fe phases in the magnetic materials except for sample Ti-M-PILC-200 which has the smallest M_s value. The presence of poorly ordered Fe phases was also considered (Bachir *et al.*, 2009). Sample Zr-M-PILC-300 has the largest M_s value. *i.e.* that sample is the most magnetic material obtained.

ZFC/FC investigation. Similar to the case of Ti-M-PILC-400 (Bachir *et al.*, 2009), the ZFC/FC curves of the three measured Al samples (Al-M-PILC-200, -400, and -500) showed very shallow distributions of blocking temperatures, T_B, and were dominated by paramagnetic behavior (Figure 5). The slight differences between ZFC and FC are indicative of the presence of non-paramagnetic contributions.

For Zr-M-PILC-200 and Zr-M-PILC-300, the ZFC/FC curves showed a broad and shallow distribution of blocking temperatures related to the presence of very weak magnetic ordering. In contrast, in the case of Zr-M-PILC-500 and Ti-M-PILC-200 (Bachir *et al.*, 2009), the plot lacked any indication of a blocking temperature. Such behavior was supported by the absence of or very minor hysteresis at all temperatures applied with the SQUID for these samples and is indicative of paramagnetic behavior.

Curie-Weiss law. Determination of θ and C. The values of the Weiss constant, θ, and the Curie constant, C, were determined by fitting the data of FC susceptibility, $\aleph_{FC}$, to the Curie-Weiss law (Morrish, 1965; Suzuki *et al.*, 2003; Bachir *et al.*, 2009) in the paramagnetic region (Table 6).

Table 5. Specific saturation magnetization of Al/Zr/Ti-M-PILCs at 300 K.

Samples	M_s (A m^2/kg of Fe added)
Al-M-PILC-200	46
Al-M-PILC-400	42
Al-M-PILC-500	41
Zr-M-PILC-200	66
Zr-M-PILC-300	72
Zr-M-PILC-500	38
Ti-M-PILC-200	8
Ti-M-PILC-400	33
Ti-M-PILC-500	57
Magnetite Fe_3O_4	90−92
Maghemite γ-Fe_2O_3	60
Fe	218
Fe_xB	~60

Table 6. Curie-Weiss-law parameters of M-PILCs.

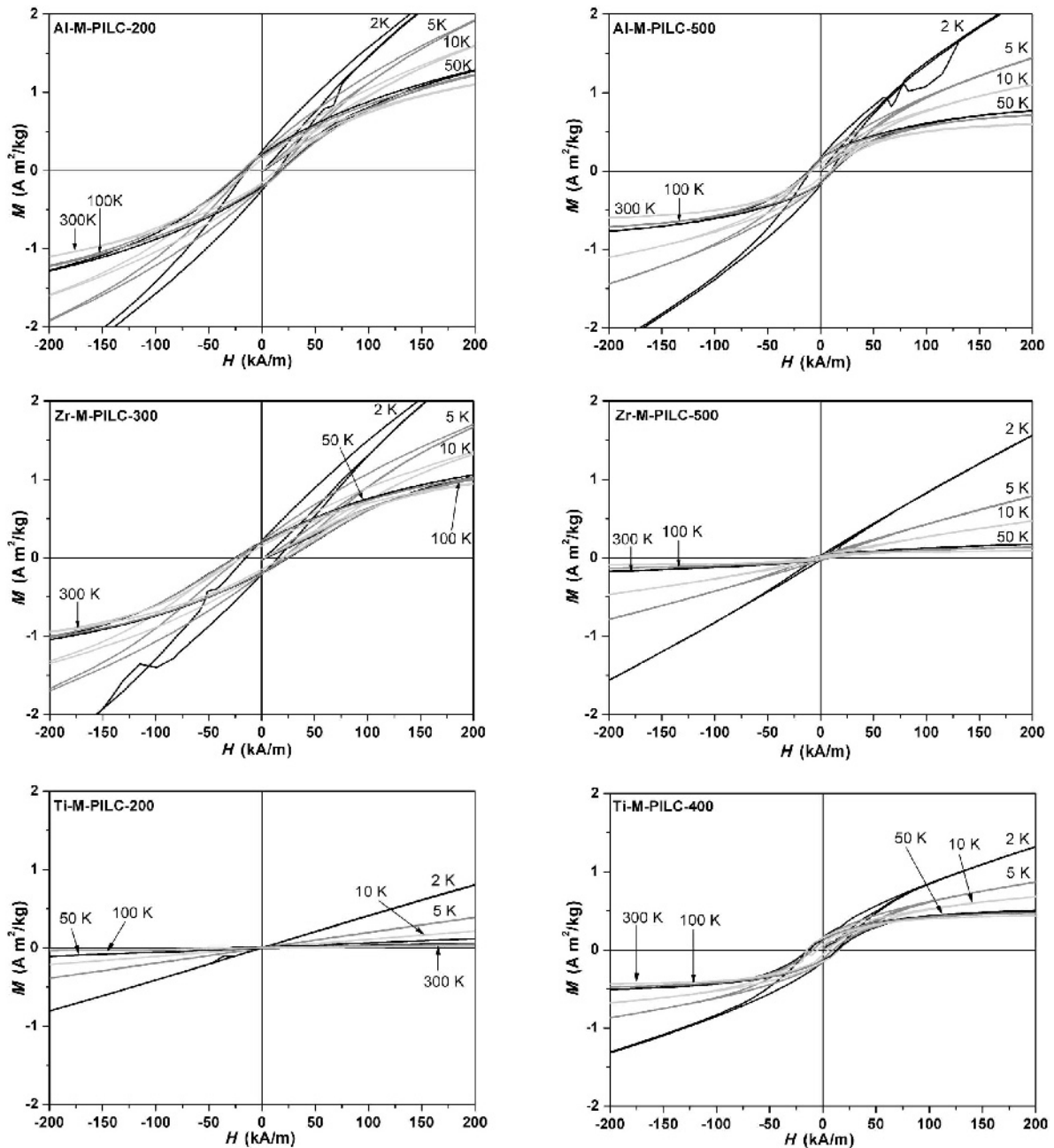| Samples	θ (K)	$C \times 10^6$ (m^3 K/kg)	R^2
Al-M-PILC-200	−1.6	26.8	0.991
Al-M-PILC-400	−1.5	29.1	0.983
Al-M-PILC-500	−1.3	27.3	0.988
Zr-M-PILC-200	−1.0	16.0	1.000
Zr-M-PILC-300	−0.6	20.3	1.000
Zr-M-PILC-500	−0.7	20.3	0.999
Ti-M-PILC-200	−0.7	12.0	1.000
Ti-M-PILC-400	−1.9	18.1	0.962
Ti-M-PILC-500	−2.3	17.3	0.931

θ: Weiss constant and C: Curie constant

Figure 4. Hysteresis curves of Al/Zr/Ti magnetic pillared clays.

The negative values of θ in all M-PILCs indicated ferromagnetic behavior in these materials. In addition, the largest θ value was from sample Ti-M-PILC-500; this finding agrees with the ZFC/FC behavior presented in a previous study (Bachir *et al.*, 2009), where a distribution of T_B was obtained. The θ values were very low for Zr-M-PILC-500 and Ti-M-PILC-200, in agreement with the dominant paramagnetic behavior of these samples observed at very low temperatures.

FF calculation

The filling factors for the respective pillared clays and their magnetic forms were determined as described above (Table 7). In the case of Al materials, a correlation was observed among the decrease in SSA (Table 3), the difference in Al content $\Delta(Al_2O_3)$ (Table 8), and the FF (Table 7). The reduction in SSA was proportional to the loss of Al_2O_3. The samples Al-M-PILC-200 and -400 showed the greatest losses. In
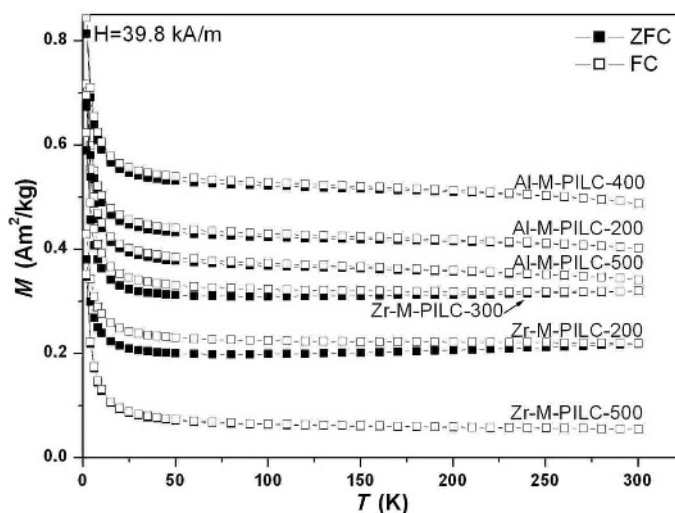
Figure 5. ZFC/FC curves of Al-M-PILC and Zr-M-PILCs. Filled symbols: ZFC; open symbols: FC curves.

addition, the FF of these samples decreased after magnetization from 0.5 to 0.3, on average, which means that after magnetization of three layers, on average, only one was intercalated with Al pillars, thus leading to a partial collapse of the pillared structure. The more calcined samples exhibited greater stability against the magnetization process (Fe intercalation and reduction by $NaBH_4$), which destabilized the pillar structure

(Table 3). In sample Al-M-PILC-500 the largest SSA and pore volume were maintained with the smallest $\Delta(Al_2O_3)$ content.

The large reduction in SSA and V_p for Zr-M-PILC-200 after magnetization (Table 3) correlated well with the corresponding difference in Zr content $\Delta(ZrO_2)$ (Table 8). This correlation was reflected in the results of the FF computation (Table 7). The corresponding FF for

Table 7. FF and IF of PILC and M-PILC.

Samples	V_p (cm^3/g)	V_{ILtheo} (cm^3/g)	V_{ILexp} (cm^3/g)	FF	IF
Al-PILC-200	0.106	0.246	0.140	0.6	2
Al-PILC-400	0.103	0.287	0.125	0.4	2
Al-PILC-500	0.103	0.261	0.125	0.5	2
Al-M-PILC-200	0.014	0.164	0.038	0.2	4
Al-M-PILC-400	0.030	0.172	0.046	0.3	4
Al-M-PILC-500	0.048	0.149	0.067	0.4	2
Zr-PILC-200	0.093	0.250	0.117	0.5	2
Zr-PILC-300	0.091	0.242	0.115	0.5	2
Zr-PILC-500	0.063	0.201	0.087	0.4	2
Zr-M-PILC-200	0.008	0.172	0.031	0.2	6
Zr-M-PILC-300	0.070	0.183	0.094	0.5	2
Zr-M-PILC-500	0.033	0.090	0.057	0.6	2
Ti-PILC-200	0.171	0.686	0.298	0.4	2
Ti-PILC-400	0.160	0.630	0.287	0.5	2
Ti-PILC-500	0.158	0.574	0.285	0.5	2
Ti-M-PILC-200	0.099	0.276	0.225	0.8	1
Ti-M-PILC-400	0.136	0.228	0.264	1.2	1
Ti-M-PILC-500	0.114	0.153	0.245	1.6	1

V_p: pore volume at $P/P_0 = 0.7$ (pore width $\leqslant 7$ nm)
V_{ILtheo}: theoretical interlayer volume
V_{ILexp}: experimental interlayer volume
FF: filling factor
IF: intercalation factor

Table 8. Difference in Al_2O_3, ZrO_2, and Al_2O_3 content (%PILCs$-$%M-PILCs).

Al samples	$\Delta(Al_2O_3)$[*]	Zr-samples	$\Delta(ZrO_2)$[#]	Ti samples	$\Delta(TiO_2)$[+]
Al-M-PILC-200	2.65	Zr-M-PILC-200	1.79	Ti-M-PILC-200	0.43
Al-M-PILC-400	2.19	Zr-M-PILC-300	0.22	Ti-M-PILC-400	-0.50
Al-M-PILC-500	1.21	Zr-M-PILC-500	0.14	Ti-M-PILC-500	-1.53

[*] difference in Al_2O_3 content (% Al-PILCs$-$% Al-M-PILCs)
[#] difference in ZrO_2 content (% Zr-PILCs$-$% Zr-M-PILCs)
[+] difference in TiO_2 content (% Ti-PILCs$-$% Ti-M-PILCs)

this sample decreased after the magnetization process from 0.5 to 0.2. In contrast, sample Zr-M-PILC-300, which had the largest M_s value, showed the smallest loss in SSA and porosity as well as a low $\Delta(ZrO_2)$ value, thus exhibiting the greatest stability. Furthermore, in the case of Ti-PILCs and the associated Ti-M-PILCs, an IF of 1 and larger was obtained (Table 7), and must be interpreted as a complete filling of the entire interlayer space, plus the precipitation of titanium oxide phases which are still associated with M-PILCs, as shown by Bachir *et al*. (2009). In this set of experiments the best calcination temperature was 400ºC, which maintained the largest SSA and pore volume values while also giving magnetic parameters suitable for magnetic application.

Mössbauer spectroscopy

Room-temperature Mössbauer spectra of Zr-M-PILC-300 and Al-M-PILC-500 (Figure 6) contained a minor ferrous doublet in addition to the ferric doublet of the parent clay, SWy-2 (Bachir *et al*., 2009). These doublets indicated that the borohydride reduction was effective in reducing part of the ferric iron (some reoxidation may also have occurred after the magnetization process). The spectra of these samples exhibited, in addition to the prominent ferric and ferrous doublets, a broad background component and, thus, an indication of a minor

sextet possibly due to the FeB/Al-Zr-alloys of different compositions (Van Wontergehm *et al.*, 1986). The high local variation in the composition presumably resulted in the absence of the resolved lines in the sextet for most samples. The room-temperature spectrum of sample Ti-M-PILC-400 reported by Bachir *et al.* (2009) had the same characteristics as those of Zr-M-PILC-300 and Al-M-PILC-500.

In order to counteract relaxational effects ensuing from small particle size ($\sim$1$-$2 nm), samples Zr-M-PILC-300 and Al-M-PILC-500 were also measured at low temperature, 3 K. The spectra obtained represented an overlap of a magnetic field distribution and two paramagnetic components (doublets) (Figure 7, Table 9). The area of the Fe(II) component was equal to that observed at room temperature, but the para-magnetic Fe(III) content decreased considerably, indicating that part of the oxidic Fe(III) is magnetically ordered at 3 K, while for Fe(II) magnetic ordering had not yet occurred. The sextet of Zr-M-PILC-300 was more pronounced than that of Al-M-PILC-500. The 3 K spectrum of Ti-M-PILC-400 exhibited the same shape as that of Ti-M-PILC-60 (Bachir *et al*., 2009), where no magnetic ordering was observed. Finally, none of the spectra investigated showed any evidence of metallic Fe, in support of the findings about the efficiency of $NaBH_4$ or re-oxidation.
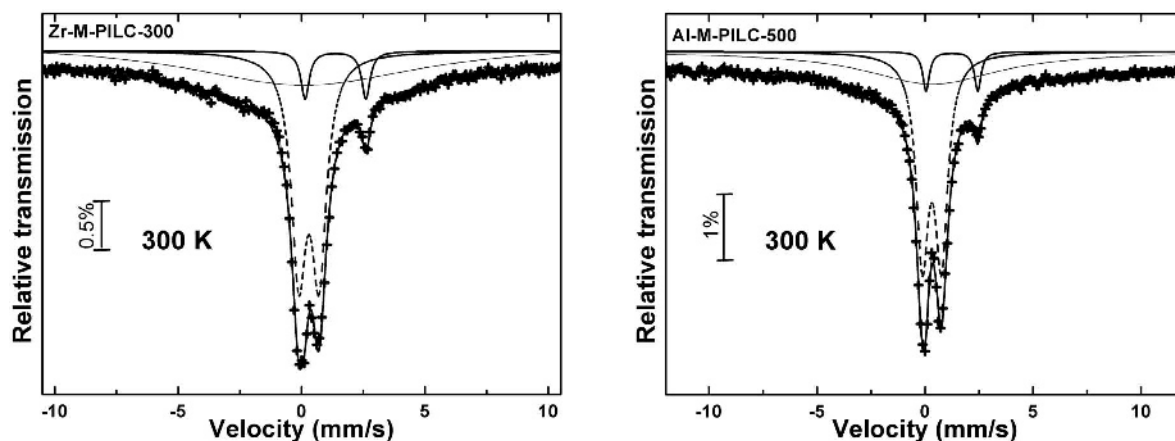

Figure 6. Room-temperature Mössbauer spectra of Al-M-PILC-500 and Zr-M-PILC-300.
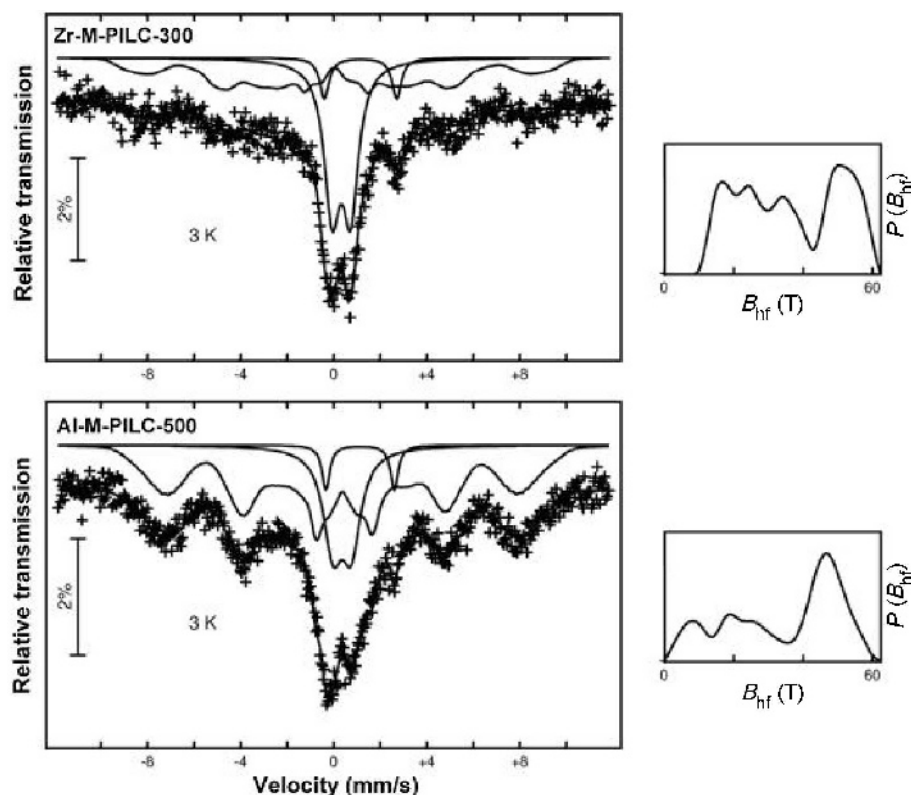
Figure 7. Low-temperature (3 K) Mössbauer spectra of Al-M-PILC-500 and Zr-M-PILC-300.

Experiments involving pure Na-SWy-2 treated with $NaBH_4$ (in the same way as with the PILCs) and subsequent examination by Mössbauer spectroscopy revealed only minor changes in the Fe(II)/Fe(III) ratio.

From the SQUID and Mössbauer measurements, the presence of magnetite, maghemite, and Fe_xB phases and poorly ordered FeB/Ti-Al-Zr-alloys of different compositions was suggested (Van Wontergehm *et al.*, 1986, Bachir *et al.*, 2009). In addition, X-ray absorption near edge spectroscopy and extended X-ray absorption fine structure experiments were carried out to further

elucidate the Fe environment, but were not part of the present study.

CONCLUSIONS

In the present study, the magnetic properties, upon Fe-intercalation and subsequent reduction by $NaBH_4$, of pillared clays obtained at different calcination temperatures were investigated. The influence of the nature of the pillars was presented. The pillared clays obtained react differently to the magnetization process as a

Table 9. Mössbauer data for Zr-M-PILC-300 and Al-M-PILC-500 at 3 K.

Samples	Fe (ox. state)	δ^{Fe} (mm/s)	ΔE_Q (mm/s)	Γ (mm/s)	Relative area (%)
Zr-M-PILC-300	III	0.44(1)	0.75(3)	0.83(7)	41.3
	II	1.12(2)	3.06(5)	0.48(7)	7.8
		Magnetic field distribution			50.9
Al-M-PILC-500	III	0.45(1)	0.82(6)	0.99(1)	27.9
	II	1.14(1)	2.96(3)	0.39(6)	4.6
		Magnetic field distribution			67.6

δ^{Fe}: Isomer shift relative to metallic Fe at room temperature
ΔE_Q: quadrupolar splitting
Γ: peak width

function of the nature of the intercalated pillar and its calcination temperature.

For all pillared clays, increase in the calcination temperature led to decreases in the CEC. This feature varied as a function of the pillar species. The corresponding CEC values followed the order: Zr-PILCs > Al-PILCs > Ti-PILCs and such behavior can be explained by the differences in the intercalated species.

After the magnetization process, SSA and porosity decreased. The reduction was different for each pillared clay and for each calcination temperature. Temperatures of 300ºC, 400ºC, and 500ºC for Zr-M-PILCs, Ti-M-PILCs, and Al-M-PILCs, respectively, were the best calcination temperatures to preserve the largest SSA and V_p values with high saturation magnetization, M_s. A comparison of the Weiss constant of the magnetic pillared clays showed that the ferrimagnetic behavior was more pronounced for Ti-M-PILC-400 and Al-M-PILC-500 than that of Zr-M-PILC-300.

In the case of Al materials, the loss of Al, $\Delta(Al_2O_3)$, at higher temperatures decreased by 1.21% for Al-M-PILC-500, confirming the stability of Al oxide pillars at 500ºC. The small $\Delta(Al_2O_3)$ value agreed with the small reduction in SSA of this sample after magnetization (57%).

In the case of Zr materials, the Zr loss, $\Delta(ZrO_2)$, decreased with increasing calcination temperature, such as a 0.22% loss in the case of Zr-M-PILC-300. For this sample, the small $\Delta(ZrO_2)$ value was in agreement with the small reduction in SSA (26%). At 300ºC the Zr pillars were not strongly affected by the magnetization process.

The FF of both samples Al-M-PILC-500 and Zr-M-PILC-300 were similar to those of the corresponding original pillared clays, confirming that these samples were not strongly affected by the magnetization process.

With regard to Ti materials, after magnetization the smallest reductions in SSA (20%) and pore volume (15%) were obtained at 400ºC. In this case the interlayer space was filled completely after magnetization.

ACKNOWLEDGMENTS

REFERENCES

Bachir, C., Lan, Y., Mereacre, V., Powell, A.K., Koch, C.B., and Weidler, P.G. (2009) Magnetic titanium pillared clays (Ti-M-PILCs): Magnetic studies and Mössbauer spectroscopy. *Clays and Clay Minerals*, **57**, 433−443.

Bartley, G.J.J. and Burch, R. (1985) Zr-containing pillared interlayer clays. Part III. Influence of method of preparation on the thermal and hydrothermal stability. *Applied*

Catalysis, **19**, 175−185.

Belessi, V., Lambropoulou, D., Konstantinou, I., Zboril, R., Tucek, J., Jancik, D., Albanis, T., and Petridis, D. (2009) Structure and photocatalytic performance of magnetically separable titania photocatalysts for the degradation of propachlor. *Applied Catalysis B: Environmental*, **87**, 181−189.

Brindley, G.W. and Brown, G. (1980) *Crystal Structures of Clay Minerals and their X-ray Identification*. Monograph **5**, Mineralogical Society, London, p. 539.

Brunauer, S., Emmett, P.H., and Teller, E. (1938) Adsorption of gases in multimolecular layers. *Journal of the American Chemical Society*, **60**, 309−319.

Chaabene, S.B., Bergaoui, L., and Ghorbel, A. (2004) Zirconium and sulphated zirconium pillared clays: a combined intercalation solution study and solid characterization. *Colloids and Surfaces A: Physicochemical Engineering Aspects*, **251**, 109−115.

Elmchaouri, A. and Mahboub, R. (2005) Effects of preadsorption of organic amine on Al-PILCs structures. *Colloids and Surfaces A: Physicochemical Engineering Aspects*, **259**, 135−141.

Köster, H.M. (1977) Die Berechnung kristallchemischer Strukturformeln von 2:1- Schichtsilikaten unter Berücksichtigung der gemessenen Zwischenschichtladungen und Kationenumtauschkapazitäten, sowie der Darstellung der Ladungsverteilung in der Struktur Mittels Dreieckskoordinaten. *Clay Minerals*, **12**, 45−54.

Lagaly, G. (1994) Layer charge determination by alkylammonium ions in layer charge characteristics of 2:1 silicate clay minerals. Pp. 1−46 in: *Layer-Charge Characteristics of 2:1 Silicate Clay Minerals* (A.R. Mermut, editor). Workshop Lecture Series, Volume, **6**. The Clay Minerals Society, Boulder, Colorado, USA.

Levin, I. and Brandon, D. (1998) Metastable Alumina Polymorphs: Crystal Structures and Transition Sequences. *Journal of the American Ceramic Society*, **81**, 1995−2012.

Mak, S.Y. and Chen, D.H. (2004) Fast adsorption of methylene blue on polyacrylic acid bound iron oxide magnetic nanoparticles. *Dyes and Pigments*, **61**, 93−98.

Meier, L.P. and Kahr, G. (1999) Determination of the cation exchange capacity (CEC) of clay minerals using the complexes of copper (II) ion with triethylenetetraamine and tetraethylenepentamine. *Clays and Clay Minerals*, **47**, 386−388.

Mishra, B.G. and Rao, G.R. (2005) Cerium containing Al- and Zr-pillared clays: Promoting effect of cerium (III) ions on structural and catalytic properties. *Journal of Porous Material*, **12**, 171−181.

Mojović, M., Daković, M., Banković, P., and Mojović, Z. (2010) Paramagnetic pillared bentonites − The new digestive tract MRI contrast agents. *Applied Clay Science*, **48**, 191−194.

Morrish, A.H. (1965) *The Physical Principles of Magnetism.* John Wiley & Sons, Inc. New York, London, Sydney.

Moskowitz, B.M. (1991) *Hitchhiker's Guide to Magnetism.* The Environmental Magnetism Workshop, Institute for Rock Magnetism, University of Minnesota, USA.

Olis, A.C., Malla, P.B., and Douglas, L.A. (1990) The rapid estimation of the layer charges of 2:1 expanding clays from a single alkylammonium ion expansion. *Clay Minerals*, **25**, 39−50.

Oliveira, L.C.A., Rios, R.V.R.A., Fabris, J.D., Garg, V.K., Sapag, K., and Lago, R.M. (2002) Activated carbon/iron oxide magnetic composites for the adsorption of contaminants in water. *Carbon*, **40**, 2177−2183.

Oliveira, L.C.A., Rios, R.V.R.A., Fabris, J.D., Sapag, K., Garg, V.K., and Lago, R.M (2003) Clay-iron oxide magnetic composites for the adsorption of contaminants in water.

Applied Clay Science, **22**, 169−177.

Rozenson, I. and Heller-Kallai, L. (1976) Reduction and oxidation of Fe^{3+} in dioctahedral smectites − 1: Reduction with hydrazine and dithionate. *Clays and Clay Minerals*, **24**, 271−282.

Rühlicke, G. and Kohler, E.E. (1981) A simplified procedure for determining layer charge by the n-alkylammonium method. *Clay Minerals*, **16**, 305−307.

Skoutelas, A.P., Karakassides, M.A., and Petridis, D. (1999) Magnetically modified Al_2O_3 pillared clays. *Chemistry of Materials*, **11**, 2754−2759.

Sterte, J. (1986) Synthesis and properties of titanium oxide cross-linked montmorillonite. *Clays and Clay Minerals*, **34**, 658−664.

Suzuki, M., Suzuki, I.S., and Walter, J. (2003) Quasi-two-dimensional magnetism in Ru and Rh metal layers sandwiched between graphene sheets. *Physical Review B*, **67**, 094406.

Van Wonterghem, J., Morup, S.J.W., Koch, C.W., Charles, S., and Wells, S. (1986) Formation of ultra-fine amorphous alloy particles by reduction in aqueous solution. *Nature*, **322**, 622−623.

Yamanaka, S. and Brindley, G.W. (1979) High surface area solids obtained by reaction of montmorillonite with zirconyl chloride. *Clays and Clay Minerals*, **27**, 119−124.

Yu, J. and Yang, Q-X., (2010) Magnetization improvement of Fe-pillared clay with application of polyetheramine. *Applied Clay Science*, **48**, 185−190.

Zhang, L. and Manthiram, A. (1996) Ambient temperature synthesis of fine metal particles in montmorillonite clay and their magnetic properties. *NanoStructured Materials*, **7**, 437−451.

Zhang, Z.D., Yu, J.L., Zheng, J.G., Skorvanek, I., Kovac, J., Dong, X.L., Li, Z.J., Jin, S.R., Yang, H.C., Guo, Z.J., Liu, W., and Zhao, X.G. (2001) Structure and magnetic properties of boron-oxide-coated Fe(B) nanocapsules prepared by arc discharge in diborane. *Physical Review B*, **64**, 024404.